

Mesoscale and Synoptic Scale Analysis of Narrow Cold Frontal Rainband during a Landfalling Atmospheric River in California during January 2021

Xun Zou¹, Jason M. Cordeira¹, Samuel M. Bartlett¹, Brian Kawzenuk¹, Shawn Roj¹, Christopher M Castellano², Chad W. Hecht³, and F. Martin Ralph⁴

¹University of California, San Diego

²Scripps Institution of Oceanography

³Scripps Institution of Oceanography, University of California, San Diego

⁴SIO

June 14, 2023

Abstract

Narrow cold-frontal rain bands (NCFR) often produce short-duration and high-intensity precipitation that can lead to flooding and debris flow in California (CA). On 27 January 2021, an atmospheric river (AR) associated with an intense surface cyclone made landfall over coastal northern CA, which featured a prominent NCFR. This study uses high-resolution West WRF simulations to accurately resolve the gap and core structure of the NCFR and provides reliable precipitation estimations, compensating for limitations of radar and satellite observations. This NCFR was supported by robust synoptic-scale quasi-geostrophic (QG) forcing for ascent and frontogenesis. It propagated southward from Cape Mendocino to Big Sur in 12 hours before stalling and rotating counter-clockwise in central/southern CA due to upstream Rossby wave breaking and amplifying upper-tropospheric trough. With the lower to middle tropospheric flow backed considerably to the south-southwest over the NCFR, the increase of the vertical wind shear caused the transition from parallel to trailing stratiform precipitation. The stall and pivot of the AR and NCFR led to intense rainfall with a 2-day precipitation accumulation greater than 300 mm over central CA. In addition, under the potential instability and frontogenesis, a moist absolutely unstable layer between 850 hPa to 700 hPa was captured at the leading edge of the NCFR, which indicated slantwise deep layer lifting and high precipitation efficiency. This study reveals synoptic-scale and mesoscale drivers of rainfall outside orographic lifting and reaffirms the importance of high-resolution numerical modeling for the prediction of extreme precipitation and related natural hazards.

Hosted file

965624_0_art_file_11070765_rvy5q1.docx available at <https://authorea.com/users/521755/articles/648926-mesoscale-and-synoptic-scale-analysis-of-narrow-cold-frontal-rainband-during-a-landfalling-atmospheric-river-in-california-during-january-2021>

Hosted file

965624_0_supp_11070760_rvy5q1.docx available at <https://authorea.com/users/521755/articles/648926-mesoscale-and-synoptic-scale-analysis-of-narrow-cold-frontal-rainband-during-a-landfalling-atmospheric-river-in-california-during-january-2021>

1 **Mesoscale and Synoptic Scale Analysis of Narrow Cold Frontal Rainband during a**
2 **Landfalling Atmospheric River in California during January 2021**

3

4 **Xun Zou, Jason M. Cordeira, Samuel M. Bartlett, Brian Kawzenuk, Shawn Roj,**
5 **Christopher Castellano, Chad Hecht, F. Martin Ralph**

6

7 CW3E, Scripps Institution of Oceanography, University of California San Diego, CA, USA

8

9

10 Corresponding authors: Xun Zou (x4zou@ucsd.edu) and Jason M. Cordeira (jcordeira@ucsd.edu)

11 **Key Points**

- 12 1. This atmospheric river caused sustained rainfall and short-duration precipitation related to a
13 narrow cold-frontal rainband.
- 14 2. The narrow cold-frontal rainband is mainly driven by synoptic-scale quasi-geostrophic
15 forcing for ascent and frontogenesis.
- 16 3. High-resolution modeling is necessary to improve the understanding and predictability of
17 high-intense short-duration precipitation.

18 **Abstract**

19 Narrow cold-frontal rain bands (NCFR) often produce short-duration and high-intensity
20 precipitation that can lead to flooding and debris flow in California (CA). On 27 January 2021,
21 an atmospheric river (AR) associated with an intense surface cyclone made landfall over coastal
22 northern CA, which featured a prominent NCFR. This study uses high-resolution West WRF
23 simulations to accurately resolve the gap and core structure of the NCFR and provides reliable
24 precipitation estimations, compensating for limitations of radar and satellite observations. This
25 NCFR was supported by robust synoptic-scale quasi-geostrophic (QG) forcing for ascent and
26 frontogenesis. It propagated southward from Cape Mendocino to Big Sur in 12 hours before
27 stalling and rotating counter-clockwise in central/southern CA due to upstream Rossby wave
28 breaking and amplifying upper-tropospheric trough. With the lower to middle tropospheric flow
29 backed considerably to the south-southwest over the NCFR, the increase of the vertical wind
30 shear caused the transition from parallel to trailing stratiform precipitation. The stall and pivot of
31 the AR and NCFR led to intense rainfall with a 2-day precipitation accumulation greater than
32 300 mm over central CA. In addition, under the potential instability and frontogenesis, a moist
33 absolutely unstable layer between 850 hPa to 700 hPa was captured at the leading edge of the
34 NCFR, which indicated slantwise deep layer lifting and high precipitation efficiency. This study
35 reveals synoptic-scale and mesoscale drivers of rainfall outside orographic lifting and reaffirms
36 the importance of high-resolution numerical modeling for the prediction of extreme precipitation
37 and related natural hazards.

38 **Plain Language Summary**

39 California often experiences short-duration, high-intensity rainfall associated with landfalling
40 atmospheric rivers (ARs), which are long, thin corridors of moisture in the atmosphere. They can
41 trigger post-fire debris flows, shallow landslides, and flash flooding. This study investigates both
42 synoptic and mesoscale precipitation characteristics of a high-impact landfalling AR in January
43 2021 based on high-resolution weather model simulations. The landfalling AR was associated
44 with an intense surface cyclone over the Northeast Pacific. It moved southward through 27
45 January prior to stalling along the central California Coast on 28 January. Due to the stalling and
46 pivoting of the AR, the coast of central and southern California experienced a long-duration
47 period of moderate precipitation, synoptic-scale forcing for ascent and short duration periods of
48 intense precipitation. In addition, the intense precipitation along the cold front can be explained
49 an effective dynamic lifting of a deep layer of atmosphere. At Las Tablas, California, this event
50 produced >375 mm of rainfall and led to a post-fire debris flow ~30 km south of Big Sur. High-
51 resolution weather modeling reveals the physical processes of precipitation and is necessary for
52 the prediction of extreme precipitation and related natural hazards.

53

54 **Key words:** Narrow Cold-frontal Rain Band (NCFR), Atmospheric River (AR), Moist

55 Absolutely Unstable Layer (MAUL), West WRF

56 **1. Introduction**

57 Atmospheric rivers (ARs) contain enhanced water vapor transport that may produce
58 extreme precipitation, benefits to water supply, and challenges to water resources management
59 across the Western U.S. (Ralph et al. 2004, 2019; Neiman et al. 2008; Kim et al. 2013). Extreme
60 precipitation associated with landfalling ARs in California is often attributed to upslope flow of
61 saturated air by a strong low-level jet stream (LLJ) in the various coastal and inland mountainous
62 terrain (e.g., the Coastal Ranges, Sierra Nevada, and Transverse Ranges, among others).
63 Orographic precipitation processes during landfalling ARs in California may also be
64 accompanied by synoptic-scale processes associated with the parent mid-latitude cyclone and
65 upstream upper-tropospheric trough, or mesoscale processes such as narrow cold frontal
66 rainbands (NCFRs; e.g., Hobbs 1978; Matejka et al. 1980; Hecht and Cordeira 2017). The
67 purpose of this study is to investigate both the synoptic and mesoscale precipitation
68 characteristics of a high-impact landfalling AR (Fig. 1a) during January 2021 that featured a
69 prominent NCFR that stalled and pivoted along the California Coast (Fig. 1b). This event
70 produced >375 mm (>15 inches) of rainfall at Las Tablas, California (Fig. 1c) and led to a post-
71 fire debris flow ~30 km south of Big Sur (Fig. 1d).

72 Many landfalling ARs in California feature short-duration, high-intensity rainfall
73 associated with NCFRs that may, given their intensity and/or antecedent conditions, trigger post-
74 fire debris flows, shallow landslides, and flash flooding (Cannon et al. 2020). These NCFRs may
75 in turn jeopardize life, property, and public infrastructure (Cannon et al. 2018; Oakley et al.
76 2018a,b). A radar- and reanalysis-based climatology of NCFRs in southern California for 1995–
77 2020 yielded 95 events (de Orla-Barile et al. 2022), including one in 2018 in Montecito (Oakley

78 et al. 2018a) that lead to 23 deaths, ~163 hospitalizations, and >\$200 million USD in direct and
79 indirect financial losses.

80 NCFRs in southern California often occur within synoptic-scale environments containing
81 mobile upper-tropospheric troughs and landfalling ARs along the California coast, robust
82 synoptic-scale quasi-geostrophic (QG) forcing for ascent, and a thermally direct lower-
83 tropospheric ageostrophic circulation related to frontogenesis (Cannon et al. 2018, 2020). These
84 NCFRs typically contain weak convective (buoyant) instability that contrasts with quasi-linear
85 convective rainbands associated with squall lines (Geerts and Hobbs 1995; Cannon et al. 2018,
86 2020). Precipitation with NCFRs is typically shallow (<3 km deep) and forced by the advance of
87 low-level cold air, convergence, and uplift of the lower-to-mid-tropospheric saturated air mass
88 containing both the AR and LLJ (Eiras-Barca et al. 2018; see Fig. 6 from Cannon et al. 2018).
89 Horizontal shear instability in the environment containing the AR and LLJ often leads to a
90 scalloped gap-and-core structure that breaks the convective line into a series of non-precipitating
91 and precipitating elements, respectively (Hobbs and Persson 1982; Browning 1986; Jorgensen et
92 al. 2003). The three-dimensional structure of an NCFR is commonly recognized as an elongated
93 band of strong reflectivity cores on radar (>40-50 dBZ) that are ~2–3 km in depth, ~3–5 km in
94 width, and up to hundreds of kilometers in length (Browning 1986; Cannon et al. 2020).

95 The shallow convective structure of NCFRs in coastal California, when combined with
96 coastal radar observation sites at elevated locations, results in challenges to observing their
97 spatial and vertical structure using National Weather Service Weather Surveillance Radar-1988
98 Doppler (WSR-88D) radars (Jorgensen et al. 2003). These challenges lead to limitations in
99 monitoring and forecasting short-duration high-intensity precipitation in locations susceptible to
100 flash flooding or debris flows such as urban areas or locations with recent burn scars. While

101 recent advances in radar technology including the deployment of C-band and X-band radars as
102 part of the Advanced Quantitative Precipitation Information (AQPI) network provide some
103 localized observations of NCFRs (i.e., over the San Francisco Bay Area), many gaps remain,
104 especially offshore. To overcome this observational gap, analysis of the NCFR in this study will
105 employ a series of high-resolution (1-km) Weather Research and Forecasting (WRF) model
106 simulations to assist in identifying the mechanisms associated with changes in synoptic-scale and
107 mesoscale precipitation characteristics during the January 2021 landfalling AR. The following
108 section 2 provides additional information on the data and methods used in this study and section
109 3 provides an overview of the landfalling AR and NCFR. Sections 4 and 5 provide a validation
110 of the WRF model simulations against observations and a concluding discussion, respectively.

111

112 **2. Data and Methods**

113 The landfalling AR and NCFR in this study are analyzed using a version of the WRF
114 model known as West-WRF (WWRF) that was developed to better describe AR characteristics
115 and their associated precipitation patterns (Martin et al. 2018). The current study uses WWRF
116 version 4.3.1 with a nested configuration that includes 9-km, 3-km, and 1-km outer, inner, and
117 local domains over coastal California (Fig. 2a). The WWRF simulations are forced and bounded
118 through nudging (every 3 hours only for domain 1) by the hourly ERA5 reanalysis dataset
119 produced by the European Centre for Medium-Range Weather Forecasts (ECMWF; Hersbach et
120 al. 2020). In total, four temporally overlapping 48-hour WWRF simulations were initialized at
121 0000 UTC on each day from 25 to 28 January 2021. Analyses in this study between 0000 UTC
122 26 January 2021 and 0000 UTC 29 January 2021 are derived from the 24-to-47-h simulation
123 times of those four simulations (see Table S1) in a manner similar to Zou et al. (2021). The

124 physical parameterizations used in the WRF simulation are listed in Table 1 and are identical
125 to those used in a study of the 2019 NCFR event in southern California and other AR-related
126 precipitation events (Cannon et al. 2018; Brandt et al. 2020).

127 The analysis of the landfalling AR and NCFR using WRF is complemented by several
128 observational and reanalysis datasets. Overland observations are provided by Automated Surface
129 Observing System (ASOS; Fovell and Gallagher 2022) stations in California that primarily
130 include hourly precipitation. Spatial analyses of different meteorological parameters are created
131 using the ECMWF ERA5 dataset, Next Generation Weather Radar (NEXRAD) data, and
132 precipitation information from the National Centers for Environmental Prediction (NCEP) Stage-
133 IV quantitative precipitation estimates (Stage-IV QPEs). The Stage-IV QPEs consist of hourly
134 precipitation data with 4-km grid spacing and can be used as a benchmark for moderate-to-heavy
135 rainfall at certain locations, especially for convective precipitation (Nelson et al. 2016). Note that
136 spatial mosaics of NEXRAD radar observations are obtained from the Multi-Radar Multi-Sensor
137 (MRMS) project (Smith et al. 2016), which combines multiple radars from the network, surface
138 observations and numerical weather prediction models.

139 To identify and quantify the strength and duration of the AR, the hourly integrated vapor
140 transport (IVT) is calculated as follows:

141
$$IVT \text{ is defined as } \left(\frac{1}{g} \int_{sfc}^{10} qu dp\right)^2 + \left(\frac{1}{g} \int_{sfc}^{10} qv dp\right)^2 \quad (1),$$

142 where g is the gravity acceleration constant ($m s^{-2}$), q is specific humidity ($kg kg^{-1}$), u and v are
143 zonal and meridional wind ($m s^{-1}$), and dp is the differential pressure (hPa). Quasi-geostrophic
144 (QG) forcing is estimated based on advanced omega equation shown as follows (Hoskins et al.
145 1978):

$$Q = f\gamma \left[\left(-\frac{\partial V_g}{\partial x} \cdot \nabla\theta \right) i, \left(-\frac{\partial V_g}{\partial y} \cdot \nabla\theta \right) j \right] \quad (2)$$

146 where γ is constant on isobaric surfaces, V_g is the geostrophic velocity, and θ is potential
 147 temperature.

148

149 **3. Results**

150 3.1 AR and NCFR overview

151 The AR initially made landfall over coastal northern California at approximately 0000
 152 UTC 27 January 2021 with a maximum IVT magnitude $>600 \text{ kg m}^{-1} \text{ s}^{-1}$ that would later persist
 153 along the coast with IVT magnitudes $>250 \text{ kg m}^{-1} \text{ s}^{-1}$ for 45 hours (Kawzenuk et al. 2023; Figs.
 154 S1 and 1a) – an AR2 according to the Ralph et al. (2019) AR scale. The landfalling AR was
 155 associated with an intense ($<988 \text{ hPa}$) surface cyclone over the Northeast Pacific that propagated
 156 southward with the landfalling AR through 27 January prior to stalling along the central
 157 California Coast on 28 January. The AR contained a prominent NCFR that migrated southward
 158 from Cape Mendocino at ~ 0300 UTC 27 January 2021, to Santa Cruz at ~ 0900 UTC 27 January
 159 2021, and Big Sur by ~ 1200 UTC 27 January 2021 prior to stalling through 28 January 2021
 160 (Figs. 3b-d). The stalling of the NCFR was accompanied by a counter-clockwise rotation or pivot
 161 of the parent landfalling AR and the band of enhanced reflectivity resulting in prolonged high-
 162 intensity precipitation over the central California coastline near the Santa Lucia Range (Figs.
 163 3b,d). The stall and pivot of the AR and NCFR over central California resulted in 2-day
 164 precipitation totals $>300 \text{ mm}$ with recurrence intervals spanning 5 to 110 years and 3-hour
 165 precipitation totals with recurrence intervals spanning 1 to 17 years (Table 2).

166

167 3.2 NCFR structure and precipitation

168 The structure of precipitation ahead of, along, and behind the NCFR changed before and
169 after it stalled and pivoted along the central California coast (Fig. 4). The observed gap-and-core
170 precipitation structure in KMUX NEXRAD radar imagery of the NCFR at 0600 UTC 27 January
171 2021 (Fig. 4e and f, inset) was simulated by the WRF composite reflectivity as a scalloped line
172 with reflectivity values >45 dBZ. The NCFR initially also contained a relatively narrow region of
173 post-frontal trailing stratiform WRF-derived composite reflectivity >30 dBZ and an extended
174 region of parallel stratiform enhanced reflectivity extending inland over central and northern
175 California at 0600 UTC 27 January 2021 (Fig. 4e). These structures occurred in association with
176 a well-defined cold-frontal boundary with coincident 10-meter wind shift (i.e., convergence) and
177 a strong southeast-to-northwest 2-m temperature gradient (Fig. 4a). Ahead of the NCFR,
178 southwest flow along the AR and LLJ at 850 hPa produced orographic precipitation in the
179 Coastal Mountains south of San Francisco through Big Sur (Figs. 4c,e). Following the stalling of
180 the AR and NCFR along the coast, the NCFR developed a larger region of post-frontal trailing
181 stratiform enhanced reflectivity offshore and over central and northern California at 0000 UTC
182 28 January 2021 (Fig. 4f). At this time, more southerly flow developed at 10 m in the cold air
183 behind the NCFR effectively decoupling the regions of strong low-level convergence and the
184 strong surface temperature gradient (Fig. 4b). Orographic precipitation continued in the
185 southwest flow along the AR and LLJ at 850 hPa ahead of the NCFR in coastal central
186 California (Figs. 4d,f).

187

188 3.3. Synoptic and mesoscale forcing mechanisms

189 The stalling and pivoting of the landfalling AR and NCFR occurred in association with
190 upstream Rossby wave breaking and an amplifying upper-tropospheric trough at 500 hPa over

191 the Northeast Pacific (Figs. 5a,b). Before the stall and upstream trough amplification, the parallel
192 stratiform region of enhanced precipitation proximal to the NCFR was collocated with a region
193 of QG forcing for ascent as illustrated by convergence of the Q-vector at 700 hPa at 0600 UTC
194 27 January 2021 (e.g., Hoskins et al. 1978; Hoskins and Pedder 1980) (Fig. 5c). Overland, it
195 appears that QG forcing for ascent occurred in association with geostrophic warm air advection
196 based on the orientation of geopotential heights and temperature in Fig. 5c and winds and
197 temperature in Fig. 4c, but offshore forcing for ascent was likely the result of differential
198 cyclonic vorticity advection by the geostrophic wind ahead of the existing upstream trough. In
199 both regions, the parallel orientation of the Q-vector with respect to potential temperature implies
200 that forcing should result in a net cyclonic rotation of the isentropes (Keyser et al. 1992)
201 consistent with the counter-clockwise pivot of the landfalling AR and NCFR. Following the stall
202 and pivot, the landfalling AR and NCFR remained juxtaposed with QG forcing for ascent related
203 to geostrophic warm air advection and differential cyclonic vorticity advection by the
204 geostrophic wind at 0000 UTC 28 January 2021 (Figs. 5b,d); however, the lower to middle
205 tropospheric flow at the surface, 850 hPa, and 700 hPa backed considerably to the south-
206 southwest over the NCFR (Figs. 4b, 4d, and 5b, respectively). The increase in vertical wind shear
207 likely influenced the transition from primarily parallel stratiform precipitation along the NCFR to
208 trailing stratiform precipitation behind the NCFR (Fig. 4f). This transition prolonged the duration
209 of intense precipitation along the California coast where the development of trailing stratiform
210 precipitation on 28 January 2021 fell in locations previously impacted by the NCFR and parallel
211 stratiform precipitation on 27 January 2021.

212 Precipitation along the NCFR was maintained by strong lower tropospheric frontogenesis
213 at 700 hPa that extended toward the south-southwest crossing the corresponding 700-hPa

214 geopotential height contours at 0600 UTC 27 January 2021 (Fig. 6a). In this way, geostrophic
215 cold air advection was effectively forcing the southeast propagation of the NCFR along the
216 California Coast leading to the uplift of the warm moist AR-related airmass ahead of the front.
217 That airmass was also weakly potentially unstable based on positive values of the 1000-850-hPa
218 equivalent potential temperature gradient (i.e., theta-e values decreasing with height; Fig. 6c). In
219 this region where frontogenesis likely promoted the release of the potential instability, the
220 WWRf model simulated a moist absolutely unstable layer (MAUL) extending from ~850 hPa to
221 700 hPa at the leading edge of the NCFR (Fig. 7). Note that previous research on MAULs
222 suggests that these unstable layers are often just a few tens of kilometers in width, persist for up
223 to 30 minutes, and occur in association with slantwise deep layer lifting (Bryan and Fritsch 2000,
224 2002). Frontogenesis along the NCFR became oriented parallel to the 700-hPa geopotential
225 height contours during the stalling that occurred by 0000 28 January 2021 with a spatial
226 decoupling of the frontal zone and regions of potential instability (Figs. 6b,d).

227 **4. Comparisons between WWRf, ERA5, and observations**

228 As expected, the 24-to-47-hour WWRf simulations bounded by and nudged with ERA5
229 reanalysis data provide similar synoptic-scale analyses (e.g., sea-level pressure and IVT
230 magnitude) of the landfalling AR along the California Coast on 27-28 January 2021 (Fig. S1).
231 Upon closer examination, comparison of the 3-hourly time series of IVT magnitudes from 26 to
232 29 January 2021 at Los Angeles (LAX) and San Francisco (SFO) illustrate that the WWRf
233 produces slightly higher IVT magnitudes during the peak in AR intensity and/or slightly longer
234 durations of intense IVT magnitudes, but is otherwise accurate with average biases of -3.3 kg m^{-1}
235 s^{-1} and $-5.7 \text{ kg m}^{-1} \text{ s}^{-1}$, respectively (Fig. S2).

236 Comparison of the WWRF precipitation with 71 overland station observations in
237 California illustrates that the statewide average correlation coefficient (r) of 1-hour accumulated
238 precipitation is 0.49 with 32.4% of stations containing an r -value >0.7 (Fig. S3a). The statewide
239 average WWRF precipitation bias is 0.01 mm, but is on average greater than 0.2 across northern
240 California (i.e., an over-prediction) and is less than -0.2 across southern California (i.e., an
241 under-prediction). Time series of hourly precipitation from the WWRF and observations at SFO,
242 LAX, and Auburn (AUN) illustrate that the WWRF is able to reasonably capture the timing and
243 peaks in precipitation; however, WWRF tends to be ~ 1 -2 hours too slow with the timing of
244 short-duration, high-intensity precipitation related to the propagation of the NCFR at SFO and
245 AUN on 27 January 2021 and at LAX on 28-29 January 2021 (Fig. S3b). Storm-total
246 precipitation from the WWRF simulation as compared to the NCEP Stage-IV QPE for the 72-h
247 period from 0000 UTC 27 January to 2300 UTC 29 January 2021 illustrates a similar pattern of
248 precipitation (Figs. S3c, d); however, the WWRF simulations underestimated the 72-h
249 accumulated precipitation in southern California in the Transverse ranges by up to 5 inches and
250 overestimated precipitation in the northern Sierra Nevada ($\sim 40^\circ\text{N}$) by ~ 4 inches.

251 The WWRF accurately simulated the gap-and-core structure of the NCFR at 0600 UTC
252 27 January 2021 offshore that matched structural elements observed by MRMS as the NCFR
253 propagated closer to the coast and within range of the coastal radar network on 27 January 2021
254 (Figs. 4e,f). In this case, the WWRF simulation provided a reasonable representation of the
255 NCFR at ranges beyond the coastal radar network due to shallow convective structure and over-
256 shooting of radar observations.

257

258 **5. Concluding discussion**

259 The landfalling AR in California in late January 2021 featured several mesoscale and
260 synoptic-scale characteristics that promoted both a long duration (>24 hours) period of moderate
261 precipitation related to sustained orographic and synoptic-scale forcing and short duration (<6-12
262 hour) periods of intense precipitation related to a NCFR. The locations that received the most
263 precipitation, influenced by both the longest duration and highest intensity rainfall, were
264 impacted by the stalling of the southward propagation of the landfalling AR and NCFR south of
265 Big Sur in the Santa Lucia Range. The stalling of the landfalling AR was accompanied by a
266 backing of IVT from west-southwest to south-southwest IVT directions and a counter-clockwise
267 pivot of the NCFR driven by upstream Rossby wave breaking and upper-tropospheric trough
268 amplification. The accompanied increase in vertical wind shear resulted in a transition from
269 primarily parallel stratiform precipitation along the NCFR to trailing stratiform precipitation
270 behind the NCFR that resulted in a prolonged period of precipitation in the location immediately
271 poleward of the front.

272 The transition from parallel stratiform precipitation to trailing stratiform precipitation in
273 the presence of increasing vertical wind shear is reminiscent of similar processes that occur
274 within some squall lines and mesoscale convective systems (Parker and Johnson 2000). Note that
275 in squall lines, the trailing stratiform precipitation is the result of environmental system-relative
276 winds at all levels that are “front-to-rear” and typically occurs in association with evaporatively
277 cooled low equivalent potential temperatures behind the front that drive the descent of a rear
278 inflow jet toward the convective zone and forward propagation (Parker and Johnson 2000). That
279 process is not observed in this case but is instead driven primarily by strong cold air advection
280 (see Fig. 6a) as described by Geerts and Hobbs (1995) as a criterion to diagnostically
281 differentiate between NCFRs and squall lines. The stalling of the NCFR into a narrow quasi-

282 stationary frontal rainband with associated southwest-to-northeast propagation of the trailing
283 stratiform and core precipitation elements along the prevailing LLJ fits the extreme-rain-
284 producing MCS archetype documented by Schumacher and Johnson (2005) as “training line -
285 adjoining stratiform.”

286 The mesoscale and synoptic-scale environment is similar to the NCFR event diagnosed
287 over southern California by Cannon et al. (2020) including featuring weak potential stability
288 released in the presence of frontogenesis and synoptic-scale forcing for ascent diagnosed via
289 convergence of the Q-vector. The analysis of synoptic-scale forcing for ascent in Cannon et al.
290 (2020) focused on the representation of the component of the Q-vector parallel to the lower
291 tropospheric potential temperature gradient (i.e., pointing toward warm air) confirming the
292 linkages across scales that support the presence of frontogenesis. Herein we focus instead on the
293 representation of the component of the Q-vector perpendicular to the lower tropospheric
294 potential temperature gradient (i.e., along the front with warm air on the right) identifying the
295 processes that supported the stalling and pivoting of the landfalling AR and NCFR. The QG
296 forcing for ascent associated with the analyzed Q-vector convergence, representative of both
297 middle tropospheric geostrophic warm air advection and differential cyclonic vorticity advection
298 by the geostrophic wind, also helps explain the observed stratiform precipitation structures along
299 and behind the NCFR in addition to hydrometeor advection related to vertical wind shear
300 discussed above. In both phases prior to and after the pivot, the best QG forcing for ascent
301 associated with Q-vector convergence was collocated with the observed regions of stratiform
302 precipitation (Fig. 7). This spatial overlap suggests that these regions of stratiform precipitation,
303 including the orographic precipitation, may have been enhanced by seeder-feeder processes (e.g.,
304 Bergeron 1965; Kingsmill et al. 2016; Hecht and Cordeira 2017).

305 The development of a MAUL in this study is not unsurprising, given the presence of
306 potential instability and frontogenesis, but their concurrence with landfalling ARs is not well
307 documented. Environments favorable for the organization of mesoscale convective systems
308 featuring MAULs (i.e., destabilization via layer lifting in the presence of saturation) typically
309 contain high moisture, CAPE, and strong low-level wind shear such as the AR diagnosed in
310 concert with two mesoscale convective systems that contributed to widespread flooding in
311 Tennessee in May 2010 (Moore et al. 2012) that coincidentally also featured trailing
312 line/adjoining stratiform precipitation structures. Note that the absence of significant CAPE
313 during a landfalling AR does not imply a MAUL cannot occur, only that lifting of the potentially
314 unstable airmass (i.e., drier air atop warmer/more moist air) resulted in differential cooling in the
315 absence of or prior to convective mixing (Bryan and Fritsch 2000). The presence of a MAUL in
316 this analysis is supported by the WRF simulation in the absence of direct observations;
317 however, rawinsonde observations featuring a MAUL during a landfalling AR in late February
318 2019 in Coastal California at Bodega Bay lend credibility to its presence in this event (Fig. S4).
319 Interestingly, while orographic processes were well forecast by the WRF model in that
320 February 2019 event, the precipitation efficiency and microphysical complexity of the
321 environment (e.g., robust saturated mesoscale forcing for ascent in concert with orographic
322 precipitation in the region of the MAUL) were likely responsible for larger-than-forecast
323 precipitation rates, higher precipitation efficiency, and resulting forecast errors in that event (not
324 shown; personal communication F. Cannon, October 2021). Both the 2019 and 2021 events
325 featuring apparent MAULs are candidates for future analysis beyond the scope of the current
326 study.

327 In summary, the landfalling AR in California in late January 2021 featured both synoptic-
328 scale and mesoscale precipitation processes related to QG forcing for ascent, upslope flow, a
329 NCFR, potential instability and a MAUL, and likely the seeder-feeder mechanism. While
330 previous studies of landfalling ARs demonstrate that differences in storm-total water vapor
331 transport directed up the mountain slope contribute 74% of the variance in storm-total rainfall
332 (Ralph et al. 2013), the current study provides some insight into the many physical processes that
333 may comprise the remaining 26% of that variance and potentially an example of a complex event
334 that would be a statistical outlier if added to the prior studies. The results of this study
335 complement previous studies on AR-related NCFR events in California by Cannon et al. (2018,
336 2020) and reaffirm the importance of using high-resolution (~1 km) numerical modeling such as
337 WRF to analyze NCFRs and enhance situational awareness of short-duration high-intensity
338 precipitation in the coastal environment along the U.S. West Coast. As in Cannon et al. (2020),
339 we emphasize the need to study a larger sample of landfalling ARs containing NCFRs from both
340 a phenomenological and numerical modeling perspective to further evaluate model deficiencies
341 in the prediction of short-duration high-intensity precipitation, flash floods, and debris flows.

342 **Acknowledgements**

343 This research was supported by the State of California, Department of Water Resources
344 Atmospheric Rivers Program Phase III (#4600014294) awards and the U.S. Army Corps of
345 Engineers Forecast Informed Reservoir Operations (FIRO) Phase 2 (#W912HZ-19-2-0023)
346 award at the Center for Western Weather and Water Extremes (CW3E) at the University of
347 California, San Diego Scripps Institution of Oceanography. We are thankful for modeling
348 support provided by Daniel Steinhoff (CW3E) and Matthew Simpson (CW3E).

349 **Open Research**

350 ERA5 and ERA5 Land reanalysis data are available at the Copernicus Climate Change Service
351 (C3S) Climate Data Store. Surface station observations are provided by Automated Surface
352 Observing System (ASOS; Fovell and Gallagher 2022) stations archived at Iowa State University
353 (<https://mesonet.agron.iastate.edu/ASOS/>). NEXRAD radar observations are obtained from the
354 Multi-Radar Multi-Sensor (MRMS) project (Smith et al 2016;
355 https://mrms.nssl.noaa.gov/qvs/product_viewer/). West WRF is developed at CW3E for weather
356 and hydrological extremes in the western U.S. (<https://cw3e.ucsd.edu/west-wrf/>).

357

358 Reference List for Open Research:

359 Fovell, R. G., and A. Gallagher, 2022: An Evaluation of Surface Wind and Gust Forecasts from
360 the High-Resolution Rapid Refresh Model. *Weather Forecast.*, **37**, 1049–1068,
361 <https://doi.org/10.1175/WAF-D-21-0176.1>.

362 Smith, T. M., and Coauthors, 2016: Multi-Radar Multi-Sensor (MRMS) Severe Weather and
363 Aviation Products: Initial Operating Capabilities. *Bull. Amer. Meteor.*, **97**, 1617–1630,
364 <https://doi.org/10.1175/BAMS-D-14-00173.1>.

365

366 **References:**

- 367 Brandt, W. T., K. J. Bormann, F. Cannon, J. S. Deems, T. H. Painter, D. F. Steinhoff, and J.
368 Dozier, 2020: Quantifying the Spatial Variability of a Snowstorm Using Differential
369 Airborne Lidar. *Water Resour. Res.*, **56**, e2019WR025331,
370 <https://doi.org/10.1029/2019WR025331>.
- 371 Browning, K. A., 1986: Conceptual Models of Precipitation Systems. *Weather Forecast.*, **1**, 23–
372 41, [https://doi.org/10.1175/1520-0434\(1986\)001<0023:CMOPS>2.0.CO;2](https://doi.org/10.1175/1520-0434(1986)001<0023:CMOPS>2.0.CO;2).
- 373 Bryan, G. H., and M. J. Fritsch, 2000: Moist Absolute Instability: The Sixth Static Stability State.
374 *Bull. Amer. Meteor.*, **81**, 1207–1230, [https://doi.org/10.1175/1520-0477\(2000\)081<1287:MAITSS>2.3.CO;2](https://doi.org/10.1175/1520-0477(2000)081<1287:MAITSS>2.3.CO;2).
- 375
- 376 Bryan, H., and M. Fritsch, 2002: The structure and dynamics of moist absolutely unstable layers
377 in a simulated squall line [poster].
- 378 Cannon, F., C. W. Hecht, J. M. Cordeira, and F. M. Ralph, 2018: Synoptic and Mesoscale
379 Forcing of Southern California Extreme Precipitation. *J. Geophys. Res. Atmos.*, **123**,
380 13,714–13,730, <https://doi.org/10.1029/2018JD029045>.
- 381 ———, and Coauthors, 2020: Observations and Predictability of a High-Impact Narrow Cold-
382 Frontal Rainband over Southern California on 2 February 2019. *Weather Forecast.*, **35**,
383 2083–2097, <https://doi.org/10.1175/WAF-D-20-0012.1>.
- 384 Cifelli, R., and Coauthors, 2022: Advanced Quantitative Precipitation Information: Improving
385 Monitoring and Forecasts of Precipitation, Streamflow, and Coastal Flooding in the San
386 Francisco Bay Area. *Bull. Amer. Meteor.*, **1**, <https://doi.org/10.1175/BAMS-D-21-0121.1>.
- 387 Eiras-Barca, J., A. M. Ramos, J. G. Pinto, R. M. Trigo, M. L. R. Liberato, and G. Miguez-Macho,
388 2018: The concurrence of atmospheric rivers and explosive cyclogenesis in the North

389 Atlantic and North Pacific basins. *Earth Syst. Dyn.*, **9**, 91–102,
390 <https://doi.org/10.5194/esd-9-91-2018>.

391 Fovell, R. G., and A. Gallagher, 2022: An Evaluation of Surface Wind and Gust Forecasts from
392 the High-Resolution Rapid Refresh Model. *Weather Forecast.*, **37**, 1049–1068,
393 <https://doi.org/10.1175/WAF-D-21-0176.1>.

394 Geerts, B., and P. V. Hobbs, 1995: A squall-like narrow cold-frontal rainband diagnosed by
395 combined thermodynamic and cloud microphysical retrieval. *Atmos. Res.*, **39**, 287–311,
396 [https://doi.org/10.1016/0169-8095\(95\)00018-6](https://doi.org/10.1016/0169-8095(95)00018-6).

397 Hecht, C. W., and J. M. Cordeira, 2017: Characterizing the influence of atmospheric river
398 orientation and intensity on precipitation distributions over North Coastal California.
399 *Geophys. Res. Lett.*, **44**, 9048–9058, <https://doi.org/10.1002/2017GL074179>.

400 Hersbach, H., and Coauthors, 2020: The ERA5 global reanalysis. *Q. J. R. Meteorol. Soc.*, **146**,
401 1999–2049, <https://doi.org/10.1002/qj.3803>.

402 Hobbs, P. V., 1978: Organization and structure of clouds and precipitation on the mesoscale and
403 microscale in cyclonic storms. *Rev. Geophys.*, **16**, 741–755,
404 <https://doi.org/10.1029/RG016i004p00741>.

405 ———, and P. O. G. Persson, 1982: The Mesoscale and Microscale Structure and organization of
406 Clouds and precipitation in Midlatitude Cyclones. Part V: The Substructure of Narrow
407 Cold-Frontal Rainbands. *J. Atmos. Sci.*, **39**, 280–295, [https://doi.org/10.1175/1520-0469\(1982\)039<0280:TMAMSA>2.0.CO;2](https://doi.org/10.1175/1520-0469(1982)039<0280:TMAMSA>2.0.CO;2).

408
409 Hoskins, B. J., and M. A. Pedder, 1980: The diagnosis of middle latitude synoptic development.
410 *Q. J. R. Meteorol. Soc.*, **106**, 707–719, <https://doi.org/10.1002/qj.49710645004>.

411 ———, I. Draghici, and H. C. Davies, 1978: A new look at the ω -equation. *Q. J. R. Meteorol. Soc.*,
412 **104**, 31–38, <https://doi.org/10.1002/qj.49710443903>.

413 Houze Jr., R. A., 2004: Mesoscale convective systems. *Rev. Geophys.*, **42**,
414 <https://doi.org/10.1029/2004RG000150>.

415 Jorgensen, D. P., Z. Pu, P. O. G. Persson, and W.-K. Tao, 2003: Variations Associated with
416 Cores and Gaps of a Pacific Narrow Cold Frontal Rainband. *Mon. Weather Rev.*, **131**,
417 2705–2729, [https://doi.org/10.1175/1520-0493\(2003\)131<2705:VAWCAG>2.0.CO;2](https://doi.org/10.1175/1520-0493(2003)131<2705:VAWCAG>2.0.CO;2).

418 Keyser, D., B. D. Schmidt, and D. G. Duffy, 1992: Quasigeostrophic Vertical Motions
419 Diagnosed from Along- and Cross-isentrope Components of the Q Vector. *Mon. Weather*
420 *Rev.*, **120**, 731–741, [https://doi.org/10.1175/1520-](https://doi.org/10.1175/1520-0493(1992)120<0731:QVMDFFA>2.0.CO;2)
421 [0493\(1992\)120<0731:QVMDFFA>2.0.CO;2](https://doi.org/10.1175/1520-0493(1992)120<0731:QVMDFFA>2.0.CO;2).

422 Kim, J., D. E. Waliser, P. J. Neiman, B. Guan, J.-M. Ryoo, and G. A. Wick, 2013: Effects of
423 atmospheric river landfalls on the cold season precipitation in California. *Clim. Dyn.*, **40**,
424 465–474, <https://doi.org/10.1007/s00382-012-1322-3>.

425 Kingsmill, D. E., P. J. Neiman, and A. B. White, 2016: Microphysics Regime Impacts on the
426 Relationship between Orographic Rain and Orographic Forcing in the Coastal Mountains
427 of Northern California. *J. Hydrometeorol.*, **17**, 2905–2922, [https://doi.org/10.1175/JHM-](https://doi.org/10.1175/JHM-D-16-0103.1)
428 [D-16-0103.1](https://doi.org/10.1175/JHM-D-16-0103.1).

429 Martin, A., F. M. Ralph, R. Demirdjian, L. DeHaan, R. Weihs, J. Helly, D. Reynolds, and S.
430 Iacobellis, 2018: Evaluation of Atmospheric River Predictions by the WRF Model Using
431 Aircraft and Regional Mesonet Observations of Orographic Precipitation and Its Forcing.
432 *J. Hydrometeorol.*, **19**, 1097–1113, <https://doi.org/10.1175/JHM-D-17-0098.1>.

433 Matejka, T. J., R. A. Houze Jr, and P. V. Hobbs, 1980: Microphysics and dynamics of clouds
434 associated with mesoscale rainbands in extratropical cyclones. *Q. J. R. Meteorol. Soc.*,
435 **106**, 29–56, <https://doi.org/10.1002/qj.49710644704>.

436 Moore, B. J., P. J. Neiman, F. M. Ralph, and F. E. Barthold, 2012: Physical Processes Associated
437 with Heavy Flooding Rainfall in Nashville, Tennessee, and Vicinity during 1–2 May
438 2010: The Role of an Atmospheric River and Mesoscale Convective Systems. *Mon.*
439 *Weather Rev.*, **140**, 358–378, <https://doi.org/10.1175/MWR-D-11-00126.1>.

440 Neiman, P. J., F. M. Ralph, G. A. Wick, Y.-H. Kuo, T.-K. Wee, Z. Ma, G. H. Taylor, and M. D.
441 Dettinger, 2008: Diagnosis of an Intense Atmospheric River Impacting the Pacific
442 Northwest: Storm Summary and Offshore Vertical Structure Observed with COSMIC
443 Satellite Retrievals. *Mon. Weather Rev.*, **136**, 4398–4420,
444 <https://doi.org/10.1175/2008MWR2550.1>.

445 Nelson, B. R., O. P. Prat, D.-J. Seo, and E. Habib, 2016: Assessment and Implications of NCEP
446 Stage IV Quantitative Precipitation Estimates for Product Intercomparisons. *Weather*
447 *Forecast.*, **31**, 371–394, <https://doi.org/10.1175/WAF-D-14-00112.1>.

448 Oakley, N. S., F. Cannon, R. Munroe, J. T. Lancaster, D. Gomberg, and F. M. Ralph, 2018a:
449 Brief communication: Meteorological and climatological conditions associated with the 9
450 January 2018 post-fire debris flows in Montecito and Carpinteria, California, USA. *Nat.*
451 *Hazards Earth Syst. Sci.*, **18**, 3037–3043, <https://doi.org/10.5194/nhess-18-3037-2018>.

452 Oakley, N. S., J. T. Lancaster, B. J. Hatchett, J. Stock, F. M. Ralph, S. Roj, and S. Lukashov,
453 2018b: A 22-Year Climatology of Cool Season Hourly Precipitation Thresholds
454 Conducive to Shallow Landslides in California. *Earth Interact.*, **22**, 1–35,
455 <https://doi.org/10.1175/EI-D-17-0029.1>.

456 de Orla-Barile, M., F. Cannon, N. S. Oakley, and F. M. Ralph, 2022: A Climatology of Narrow
457 Cold-Frontal Rainbands in Southern California. *Geophys. Res. Lett.*, **49**, e2021GL095362,
458 <https://doi.org/10.1029/2021GL095362>.

459 Pandya, R. E., and D. R. Durran, 1996: The Influence of Convectively Generated Thermal
460 Forcing on the Mesoscale Circulation around Squall Lines. *J. Atmos. Sci.*, **53**, 2924–2951,
461 [https://doi.org/10.1175/1520-0469\(1996\)053<2924:TIOCGT>2.0.CO;2](https://doi.org/10.1175/1520-0469(1996)053<2924:TIOCGT>2.0.CO;2).

462 Parker, M. D., and R. H. Johnson, 2000: Organizational Modes of Midlatitude Mesoscale
463 Convective Systems. *Mon. Weather Rev.*, **128**, 3413–3436, [https://doi.org/10.1175/1520-0493\(2001\)129<3413:OMOMMC>2.0.CO;2](https://doi.org/10.1175/1520-0493(2001)129<3413:OMOMMC>2.0.CO;2).

465 Ralph, F. M., P. J. Neiman, and G. A. Wick, 2004: Satellite and CALJET Aircraft Observations
466 of Atmospheric Rivers over the Eastern North Pacific Ocean during the Winter of
467 1997/98. *Mon. Weather Rev.*, **132**, 1721–1745, [https://doi.org/10.1175/1520-0493\(2004\)132<1721:SACAOO>2.0.CO;2](https://doi.org/10.1175/1520-0493(2004)132<1721:SACAOO>2.0.CO;2).

469 Ralph, F. M., T. Coleman, P. J. Neiman, R. J. Zamora, and M. D. Dettinger, 2013: Observed
470 Impacts of Duration and Seasonality of Atmospheric-River Landfalls on Soil Moisture
471 and Runoff in Coastal Northern California. *J. Hydrometeorol.*, **14**, 443–459,
472 <https://doi.org/10.1175/JHM-D-12-076.1>.

473 Ralph, F. M., J. J. Rutz, J. M. Cordeira, M. Dettinger, M. Anderson, D. Reynolds, L. J. Schick,
474 and C. Smallcomb, 2019: A Scale to Characterize the Strength and Impacts of
475 Atmospheric Rivers. *Bull. Amer. Meteor.*, **100**, 269–289, <https://doi.org/10.1175/BAMS-D-18-0023.1>.

476

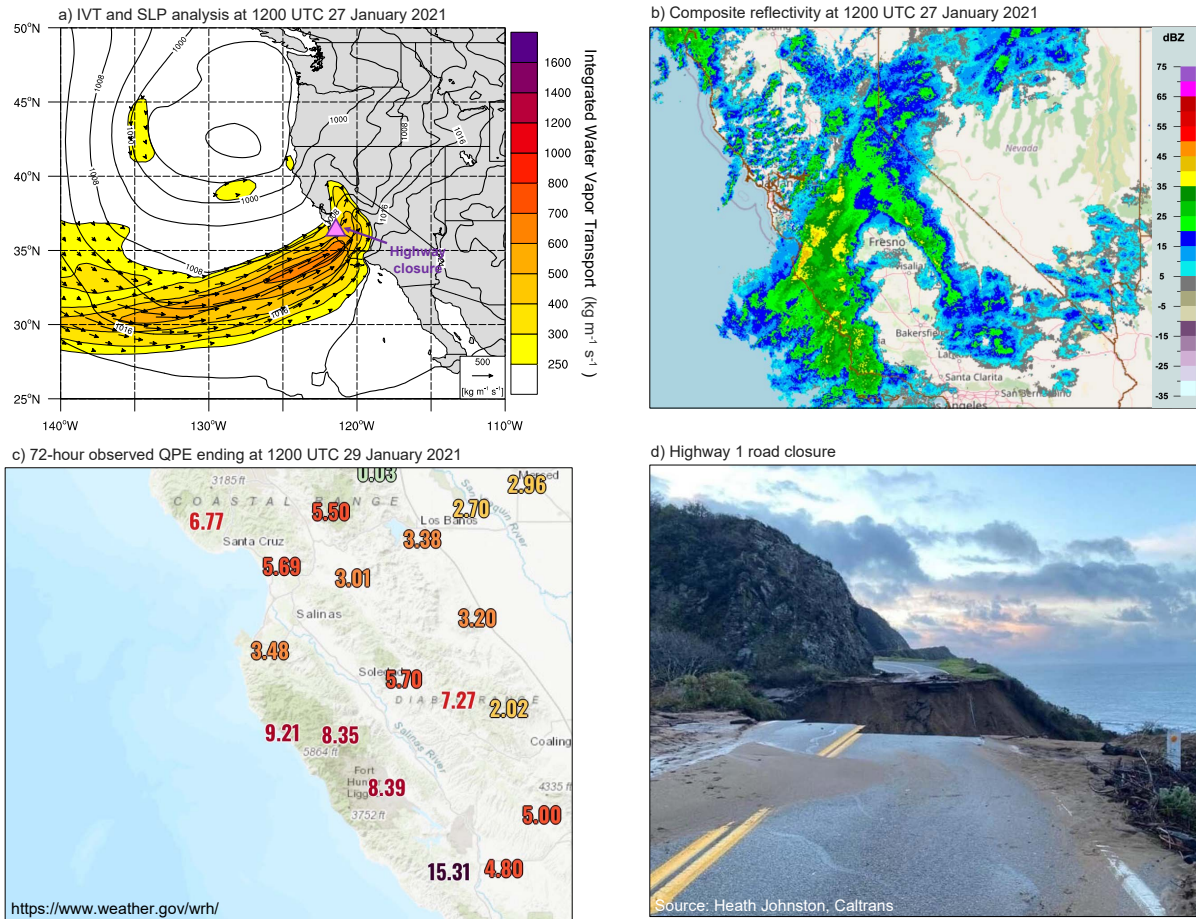
477 Schmidt, J. M., and W. R. Cotton, 1990: Interactions between Upper and Lower Tropospheric
478 Gravity Waves on Squall Line Structure and Maintenance. *J. Atmos. Sci.*, **47**, 1205–1222,
479 [https://doi.org/10.1175/1520-0469\(1990\)047<1205:IBUALT>2.0.CO;2](https://doi.org/10.1175/1520-0469(1990)047<1205:IBUALT>2.0.CO;2).

480 Schumacher, R. S., and R. H. Johnson, 2005: Organization and Environmental Properties of
481 Extreme-Rain-Producing Mesoscale Convective Systems. *Mon. Weather Rev.*, **133**, 961–
482 976, <https://doi.org/10.1175/MWR2899.1>.

483 Smith, T. M., and Coauthors, 2016: Multi-Radar Multi-Sensor (MRMS) Severe Weather and
484 Aviation Products: Initial Operating Capabilities. *Bull. Amer. Meteor.*, **97**, 1617–1630,
485 <https://doi.org/10.1175/BAMS-D-14-00173.1>.

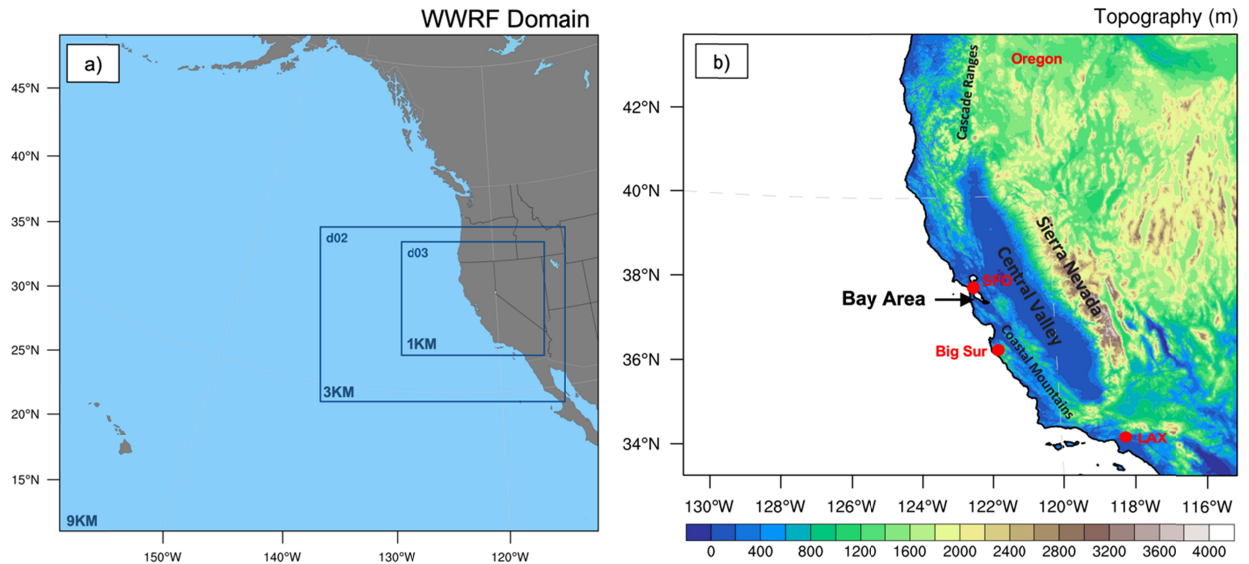
486 Zou, X., D. H. Bromwich, A. Montenegro, S.-H. Wang, and L. Bai, 2021: Major surface melting
487 over the Ross Ice Shelf part I: Foehn effect. *Q. J. R. Meteorol. Soc.*, **147**, 2874–2894,
488 <https://doi.org/10.1002/qj.4104>.

489

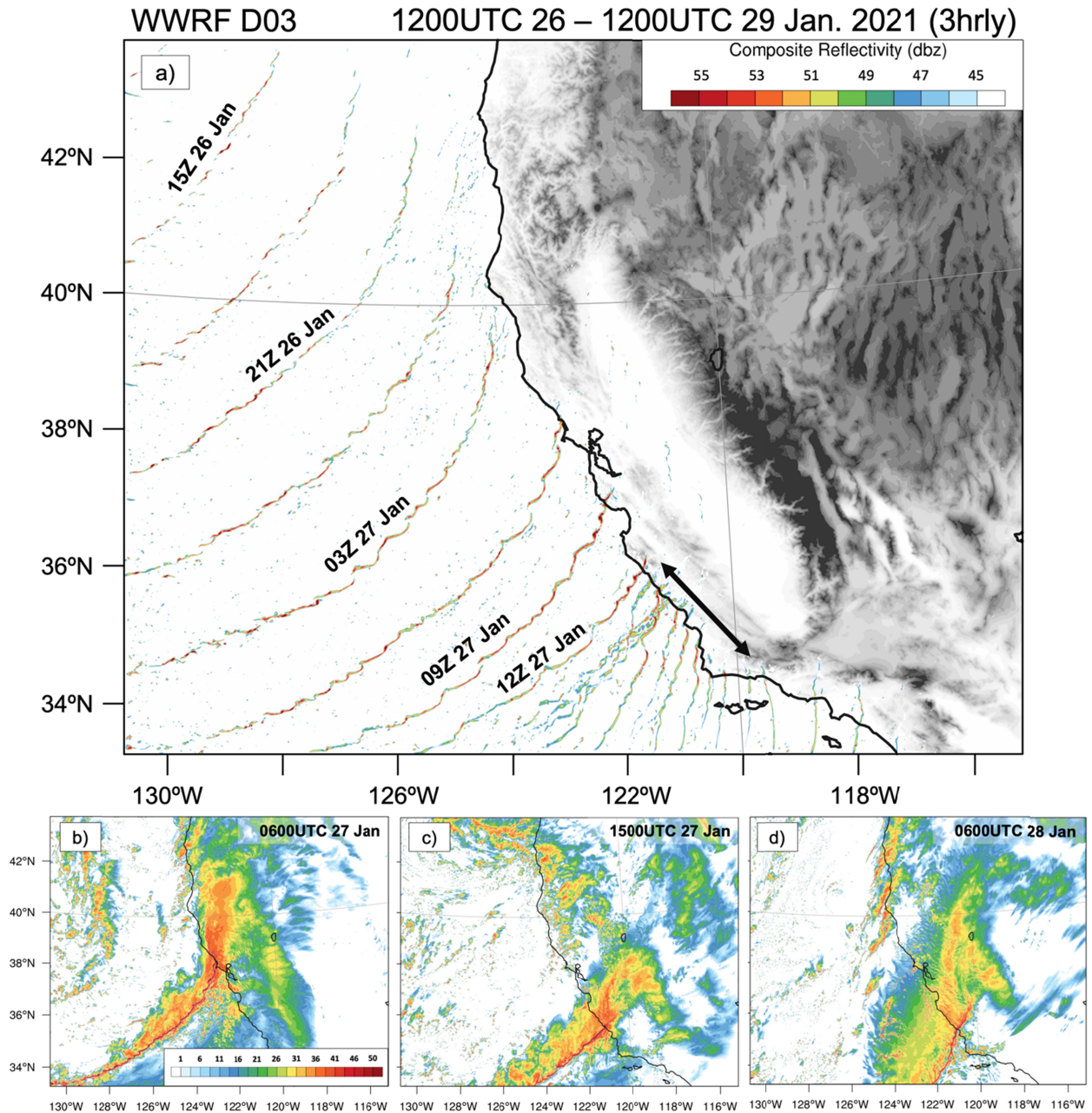


490
491
492
493
494
495
496

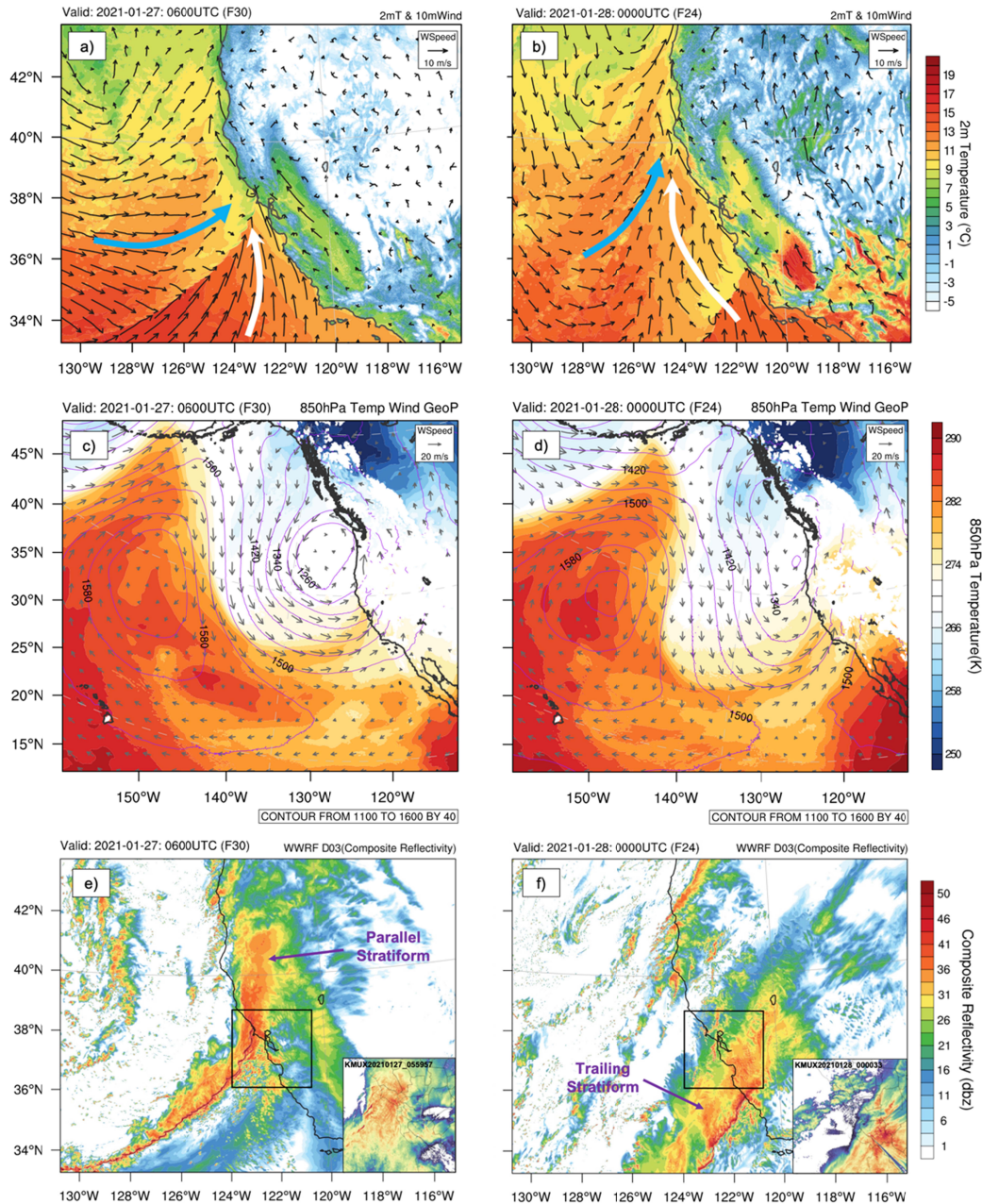
Figure 1. The overview of the 2021 NCFR event. a) Integrated vapor transport (IVT; filled contours and vectors; $\text{kg m}^{-1} \text{s}^{-1}$ and mean sea level pressure (SLP; gray contours; hPa) at 1200 UTC 27 January from ERA5 reanalysis data. b) composite reflectivity from MRMS operational product viewer at 1200 UTC 27 January. c) 72-h observed precipitation (inches) from NWS network; d) Highway 1 closure near Big Sur caused by landslide.



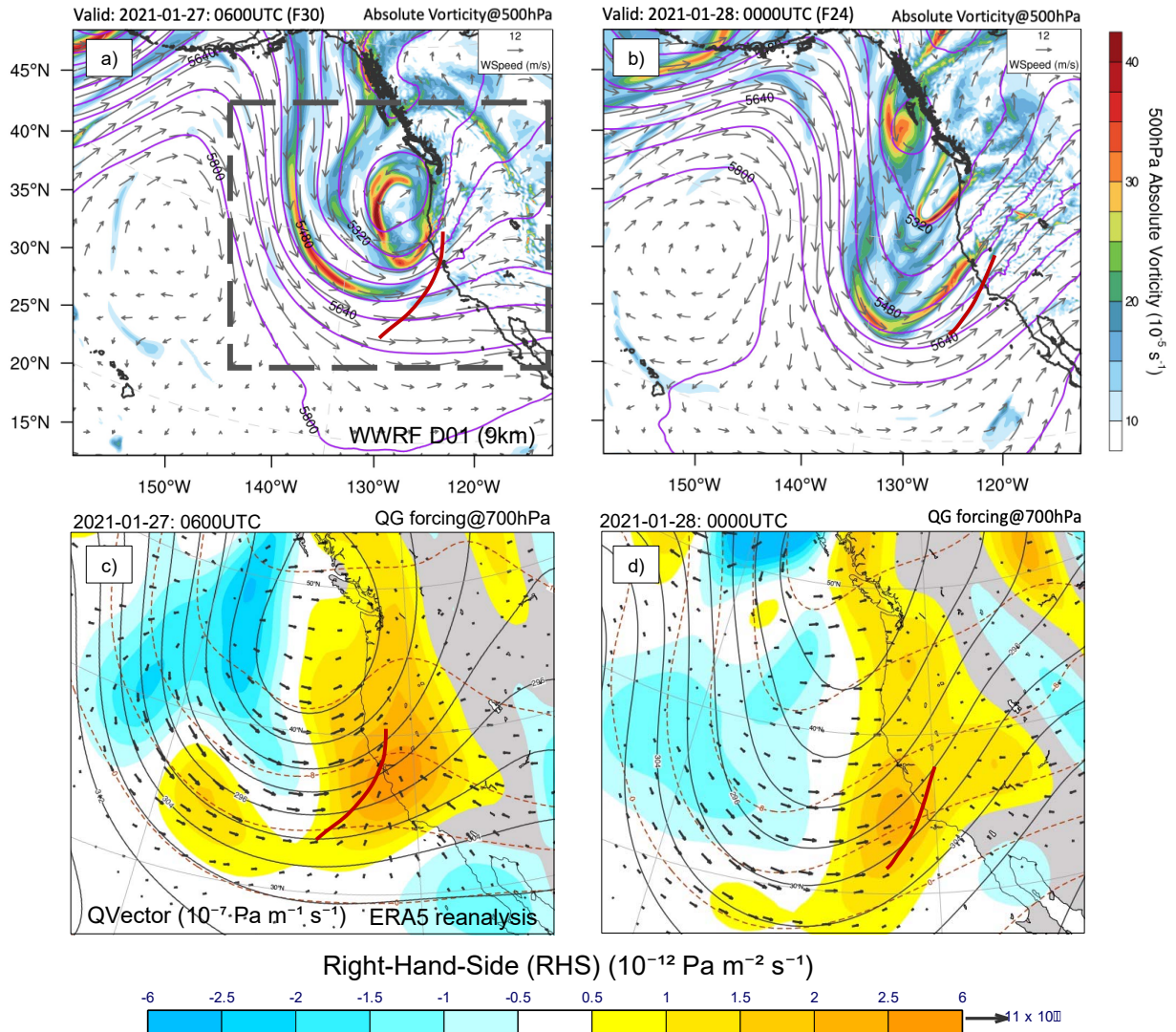
497
 498 **Figure 2.** Study area of the 2021 January NCFR case. a) Three WRF domains selected for this
 499 study. b) Topography over the study area.
 500



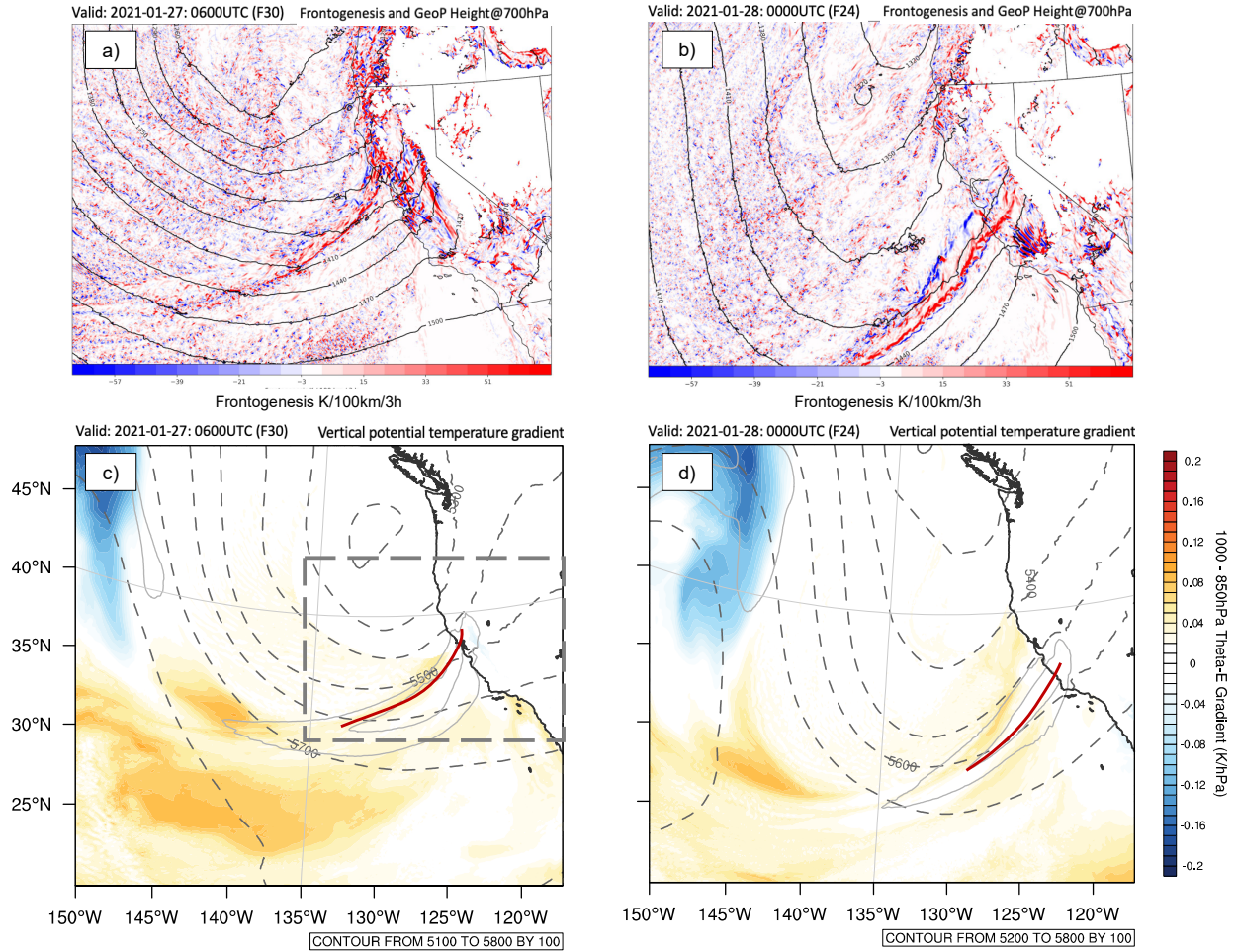
501
 502 **Figure 3.** Overview of the 2021 January NCFR event. a) Three hourly NCFR positions based on
 503 WWRF D03 simulations from 1200UTC 26 to 1200UTC 29 January 2023. b) – d) Composite
 504 reflectivity from WWRF D03 simulations at 0600UTC 26 January, 1500UTC 27 January, and
 505 0600UTC 28 January.



506
 507 **Figure 4.** Parallel stratiform (PS) precipitation and trailing stratiform (TS) precipitation during
 508 the 2021 January NCFR event. a) and b) 2-m temperature and 10-m wind from WRF D03
 509 (1km) at 0600 UTC 27 January (PS) and 0000 UTC 28 January (TS), respectively. Blue arrow
 510 represents cold air advection, and white arrow represents warm air advection. c) and d) 850-hPa
 511 geopotential height (contour line), temperature (contour fill), and wind field (vector) from
 512 WRF D01 (9km) at 0600 UTC 27 January and 0000 UTC 28 January, respectively. e) and f)
 513 Composite reflectivity from WRF D03 (1km) at 0600 UTC 27 January and 0000 UTC 28
 514 January, respectively. The subplot at the right corner in c) and d) are NEXRAD observations at
 515 San Francisco station (KMUX). Black boxes in c) and d) represent the domain of the subplots.

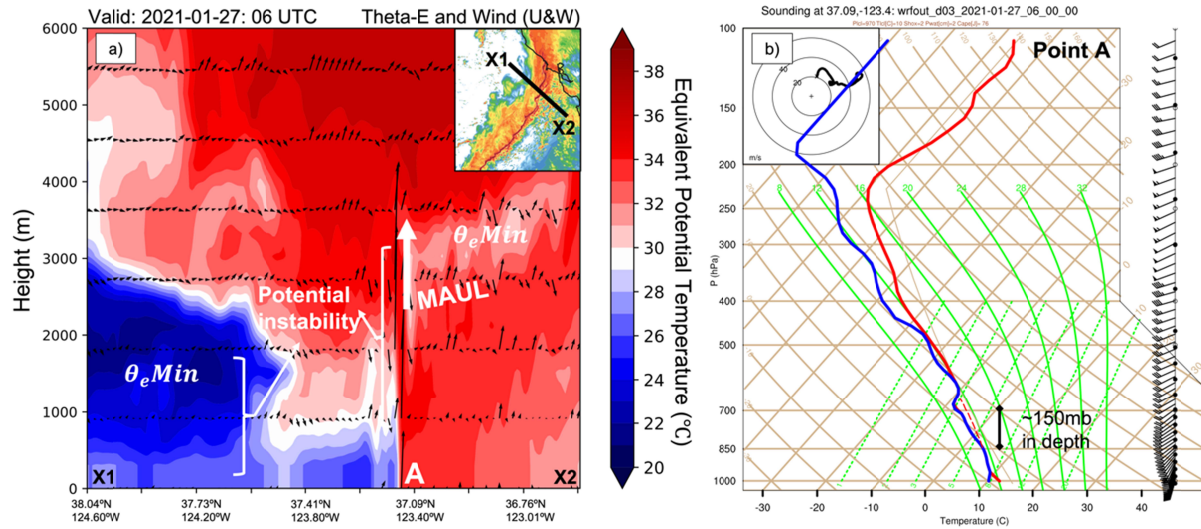


516
 517 **Figure 5.** Synoptic forcing during both PS and TS precipitation based on WWRf D01
 518 simulations and ERA5 reanalysis data. a) and b) 500hPa absolute vorticity (contour fill),
 519 geopotential height (solid purple line), and wind field (vector) at 0600 UTC 27 and 0000 UTC 28
 520 January, respectively. c) and d) 700hPa right-hand-side value calculated based on Omega
 521 equation (contour fill), geopotential height (solid black line), and temperature (dashed red line) at
 522 0600 UTC 27 and 0000 UTC 28 January, respectively. The solid red line represents the location
 523 of the NCFR. Dashed gray box in a) represents the domain in c) and d).



524

525 **Figure 6.** Mesoscale forcing during both PS and TS precipitation. a) and b) 700hPa geopotential
 526 height (contour line) and frontogenesis (contour fill) from WRF D02 at 0600UTC 27 January
 527 and 0000UTC 28 January, respectively. c) and d) 500hPa geopotential height (contour line)
 528 equivalent potential temperature gradient (contour fill) between 850-1000 hPa from WRF D01
 529 at 0600UTC 27 January and 0000UTC 28 January, respectively. Grey solid lines in c) and d)
 530 indicate AR location (IVT > 250 kg m⁻¹ s⁻¹). Red solid lines in c) and d) indicate the location of
 531 NCFR. Grey dashed box in c) represents the domain in a) and b).
 532



533
 534 **Figure 7.** Moist absolutely unstable layers (MAUL) captured in WRF D03 simulations at
 535 0600UTC 27 January 2023. a) Cross-section of equivalent potential temperature and wind (u, w).
 536 Subplot at the top right corner is the composite reflectivity with the location of cross-section
 537 (black line; X1X2). b) Skew-T plot at location A labeled in a).
 538

539 **Table 1.** WWRF model setting.

	WWRF V4.3.1
Input data	ECMWF reanalysis data (ERA5)
Horizontal resolution	9 km / 3 km / 1 km
Vertical levels	100 levels
Temporal resolution	30min
Spin-up	24h
Microphysics	Thompson
PBL scheme	YSU scheme
Shortwave and longwave	Both RRTMG
Land surface options	Noah-MP land surface model
Surface layer options	Monin-Obukhov Similarity scheme
Cumulus options	Grell-Devenyi ensemble scheme

540

541 **Table 2.** Observed Total Precipitation Accumulations Compared to Historical Records.

Location	2-day Total Accumulations (mm)	Average Recurrence Interval	Max 3-hour Total Accumulations (mm)	Average Recurrence Interval
San Cruz, CA	130.05	~7 years	30.74	~2 years
Monterey, CA	79.03	~7 years	25.40	~2 years
Millers Ranch, CA	195.83	~15 years	29.97	~1.25 years
Bryson, CA	339.60	~110 years	60.96	~17 years
San Luis Obispo, CA	107.45	~5 years	22.35	<1 year

542 *2-day total accumulation and max 3-hour total accumulations are from CDEC stations and
 543 ASOS stations archived at University of Utah MesoWest dataset ([https://mesowest.utah.edu/cgi-](https://mesowest.utah.edu/cgi-bin/droman/download_api2.cgi)
 544 [bin/droman/download_api2.cgi](https://mesowest.utah.edu/cgi-bin/droman/download_api2.cgi)). Precipitation frequency (PF) is calculated based on frequency
 545 analysis of partial duration series (PDS) via NOAA Atlas, Volume 6, Version 2 dataset
 546 (https://hdsc.nws.noaa.gov/hdsc/pfds/pfds_map_cont.html). Average recurrence intervals are
 547 estimated based on the PF value of 3-hour and 2-day accumulations.